crystals

MDPI

Article

A New Zero-Dimensional $(CsK_2)BiCl_6$ Metal Halide: Boosting Emission via B-Site Mn-Doping

Jie Wu, Shuai Zhang, Jun Yan, Bingsuo Zou and Ruosheng Zeng *

School of Physical Science and Technology, MOE Key Laboratory of New Processing Technology for Non-Ferrous Metals and Materials, Guangxi Key Laboratory of Processing for Non-Ferrous Metals and Featured Materials, Guangxi University, Nanning 530004, China

* Correspondence: zengrsh@guet.edu.cn

Abstract: The A site of zero-dimensional (0D) metal halides A_3BiCl_6 can be replaced by Cs and/or K, thus, four possible 0D A_3BiCl_6 forms exist, such as $(Cs_2K)BiCl_6$, $(CsK_2)BiCl_6$, K_3BiCl_6 and Cs_3BiCl_6. It is well known that Cs_3BiCl_6 has been reported. We predict that both $(Cs_2K)BiCl_6$ and K_3BiCl_6 do not have enough structural and thermodynamic stability, but $(CsK_2)BiCl_6$ should be a 0D stable A_3BiCl_6 candidate based on density functional theory (DFT). Furthermore, 0D $(CsK_2)BiCl_6$ metal halide was experimentally prepared by the solvothermal method. Though $(CsK_2)BiCl_6$ metal halide exhibits an indirect bandgap and poor luminescence properties, the emission can be boosted by B-site Mn-doping due to the efficient energy transfer from self-trapped excitons (STE) to the d-state of Mn ions. Our results enrich the family of 0D bi-based metal halides and provide guidance for the regulation of the structural and optical properties of metal halides.

Keywords: zero-dimensional; density functional theory; Mn-doping

Citation: Wu, J.; Zhang, S.; Yan, J.; Zou, B.; Zeng, R. A New Zero-Dimensional $(CsK_2)BiCl_6$ Metal Halide: Boosting Emission via B-Site Mn-Doping. *Crystals* **2022**, *12*, 1681. https://doi.org/10.3390/cryst12111681

Academic Editor: Dmitri Donetski

Received: 31 October 2022
Accepted: 19 November 2022
Published: 21 November 2022

1. Introduction

Lead halide perovskites with the chemical formula $APbX_3$ ($A = Cs^+$, Rb^+, X = Cl, Br, and I) have developed rapidly in recent years due to their unique optoelectronic properties, and they are widely used in various fields, such as solar cells, light-emitting diodes (LEDs), X-ray detectors, etc. [1–13]. At present, all-inorganic perovskites have been extensively studied, and different types of perovskites can exhibit different optical properties, which determine the direction of their application in devices [14–16]. For example, for solar cell devices, a high-dimensional perovskite structure is required as the emission layer of the cell. Highly interconnected octahedrons have a higher effective carrier mass and better electron space transport. This will directly affect the photoelectric conversion efficiency of the device [17–22]. Efficient emission of perovskite is an important requirement for the high external quantum efficiency of LED devices. If perovskite light-emitting layers are chosen for the preparation of LED devices, low-dimensional metal halides are a suitable choice [23–27]. Compared with three-dimensional (3D) perovskites, low-dimensional perovskites have better luminescence properties, especially zero-dimensional (0D) perovskites, whose isolated octahedron characteristics can effectively localize photogenerated carriers and further increase the probability of radiation recombination. As a result, most zero-dimensional metal halides exhibit ultra-high photoluminescence quantum efficiency and are candidate materials for a new generation of LED and display devices [28–31].

Compared with 3D perovskites, 0D perovskites exhibit unique crystal structures due to their metal halide, with regular octahedra being completely isolated by monovalent cations [32–34]. Therefore, it exhibits strong quantum confinement and exciton-phonon interaction, resulting in exciton localization and the formation of self-trapped exciton states. This unique electronic structure makes it exhibit excellent optoelectronic device performance and has a wide range of application prospects [35–38]. In 2016, M. Bakr et al. synthesized a 0D Cs_4PbBr_6 perovskite nanocrystal with a high PLQY of 45%, which is

much higher than that of 3D perovskites [39]. However, the inherent toxicity and poor environmental stability of lead-based halide perovskites still hinder practical applications. The most common method is to use trivalent ions (Sb^{3+}, In^{3+}, and Bi^{3+}) instead of divalent Pb ions to form low-dimensional nontoxic metal halides, such as $Cs_3A_2X_9$ or Cs_3AX_6 (A = Sb, In, Bi; X = Cl, Br, and I) [40–42]. In 2017, Tang et al. synthesized new all-inorganic 0D $Cs_3Sb_2Br_9$ blue light quantum dots by the ligand-assisted recrystallization method [43]. It has a high PLQY of 46%, and the mechanism of luminescence enhancement is mainly due to the quantum well band structure and its larger exciton binding energy, which effectively improves the radiative recombination efficiency. Additionally, the 0D In-based halide perovskite $Cs_2InBr_5 \cdot H_2O$ shows red emission with a PLQY of 33% [44], and emits yellow emission after heating to dehydrate the material, showing the unique property of sensitive water detection. Regarding Bi-based halide perovskites, the research on 2D Bi-based halide perovskites has progressed rapidly, while the corresponding 0D materials have progressed slowly. In 2020, Chen et al. used benzoyl halides as halide precursors, and synthesized homogeneous Cs_3BiX_6 NCs by the heat injection method [1]. We have also recently reported that a moderate amount of Mn-doping can effectively enhance the orange broadband emission of Cs_3BiCl_6 by the breaking bandgap transition [40]. However, there are few reports on the A-site regulation of 0D Cs_3BiCl_6 components on the effects of the crystal structure and optical properties.

In this work, we have applied DFT calculations to study the structure and stability of different A sites of A_3BiCl_6, such as $(Cs_2K)BiCl_6$, $(CsK_2)BiCl_6$, K_3BiCl_6 and Cs_3BiCl_6. Our results show that $(CsK_2)BiCl_6$ has good structural and thermodynamic stability, but it exhibits an indirect bandgap and poor optical properties., while $(Cs_2K)BiCl_6$ and K_3BiCl_6 cannot form stable structures. Mn-doping in $(CsK_2)BiCl_6$ can change the energy band structure of $(CsK_2)BiCl_6$ and improve its optical properties. Furthermore, on the basis of theoretical calculations, we further synthesized $(CsK_2)BiCl_6$ metal halides by the solvothermal method, and further regulated the optical properties by Mn-doping. The results show that the PLQY of Mn-doped $(CsK_2)BiCl_6$ are greatly improved, and a broadband bright orange-yellow emission at 605 nm is achieved. Our DFT calculations provide a good prediction of the optical properties and structural stability of the 0D $(CsK_2)BiCl_6$, which enrich the structural composition of 0D Bi-based lead-free metal halides, and can help to accelerate the development of an environmentally stable 0D Bi-based halide perovskite derivative.

2. Result and Discussion

2.1. Theoretical Prediction of Crystallographic and Thermodynamic Stabilities of 0D A_3BiCl_6

The first-principle calculations were carried out using density functional theory with a plane-wave basis set and projector-augmented wave (PAW) method [45,46] as implemented in the Vienna ab initio simulation package (VASP). The geometries and electronic structures were relaxed by the generalized gradient approximation (GGA) in the modified Perdew–Burke–Ernzerhof (PBE) form [47–49]. A kinetic-energy cutoff of 350 eV was tested and found to be sufficient for plane-wave expansion to achieve good convergence. The conjugate gradient algorithm was used until the total energy was converged to 10^{-5} eV in the electronic self-consistency loop, and a force criterion of 0.01 eV Å was allowed. There were 40 atoms in the A_3BX_6 simulation unit and k points were set as $7 \times 7 \times 4$.

First, we constructed the 0D structures of $(Cs_2K)BiCl_6$, $(CsK_2)BiCl_6$, and K_3BiCl_6 through the regulation of the A site (Figure 1). The 0D $(Cs_2K)BiCl_6$, $(CsK_2)BiCl_6$, and K_3BiCl_6 are monoclinic crystal structures with space group C/2c, consistent with 0D Cs_3BiCl_6. In $(CsK_2)BiCl_6$, the $BiCl_6^{3-}$ octahedron is sterically isolated by surrounding Cs^+ and K^+ atoms. The distance between two adjacent Bi atoms in $(CsK_2)BiCl_6$ is approximately 7.71–7.76 Å, indicating almost no interaction between the two adjacent $BiCl_6^{3-}$ octahedra and the nature of 0D electronic dimensionality [50].

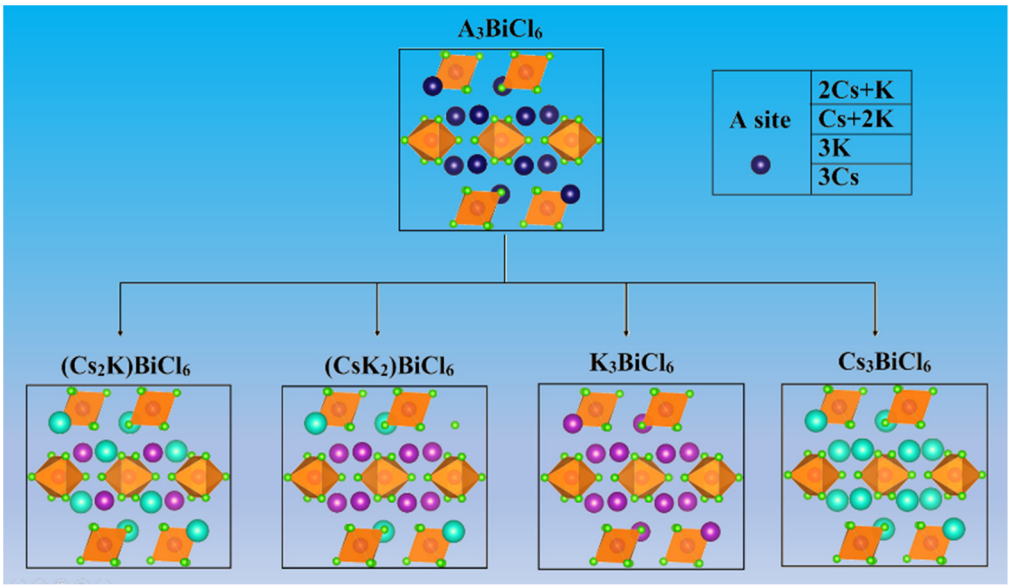

Figure 1. A-site regulation of 0D A_3BiCl_6.

The Goldschmidt empirical criterion was used to evaluate the crystal stability of perovskite structure materials [51,52]. Thus, two empirical quantities were obtained: the Goldschmidt tolerance factor (t) and the octahedral factor (μ). Previous statistical analysis of all existing halide perovskites has shown that stable perovskite structure formation requires $0.81 < t < 1.11$ and $0.41 < \mu < 0.90$. Due to the existence of multiple cations, the formulas for t and μ in this paper can be defined as:

$$\mu = r_{Bi}/r_{Cl} \quad (1)$$

$$t_{Cs_{3-x}K_xBiCl_6} = \left\{ \frac{(3-x)r_{Cs} + xr_K}{3} + r_{Cl} \right\} / \sqrt{2}(r_{Bi} + r_{Cl}) \quad (2)$$

where r_{Cs}, r_K, r_{Bi} and r_{Cl} are the Shannon ionic radii of Cs^+, K^+, Bi^{3+} and Cl^- ions, respectively. The t and μ of the four structures are shown in Figure 2. Our calculations show that both t and μ of Cs_3BiCl_6, $(Cs_2K)BiCl_6$ and $(CsK_2)BiCl_6$ are within reasonable ranges, indicating that the Cs_3BiCl_6, $(Cs_2K)BiCl_6$ and $(CsK_2)BiCl_6$ compounds are stable perovskite structures. Although K_3BiCl_6 has a $\mu = 0.569$, within the recommended range, its t-value of 0.794 suggests that it may form a distorted perovskite structure.

Then, to further evaluate the thermodynamic stabilities of these structures, we calculated their decomposition enthalpies (ΔH_d) with respect to possible decomposition pathways. ΔH_d is defined as the energy difference between the decomposed producers and the A_3BiCl_6 compound. The large positive values of ΔH_d (decomposed into corresponding binary materials) above 20 meV per atom indicate the thermodynamic stability of the A_3BiCl_6 compounds. In the stability assessment, including the possibility of decomposition pathways involving ternary compounds is quite important for quaternary compounds. Therefore, in our calculations, we considered the expected decomposition products reported experimentally, including selected ternary compounds. For $(CsK_2)BiCl_6$, we have investigated the following possible decomposition pathways:

$$(CsK_2)BiCl_6 \rightarrow CsCl + BiCl_3 + 2KCl \quad 82.23 \text{ meV/atom} \quad (3)$$

$$(CsK_2)BiCl_6 \rightarrow {}^1/_3\, Cs_3BiCl_6 + {}^2/_3\, BiCl_3 + 2KCl \quad 65.61 \text{ meV/atom} \quad (4)$$

$$(CsK_2)BiCl_6 \rightarrow {}^1/_3\, Cs_3Bi_2Cl_9 + {}^1/_3\, BiCl_3 + 2KCl \quad 21.96 \text{ meV/atom} \quad (5)$$

The reaction pathways for Cs_3BiCl_6, $(Cs_2K)BiCl_6$ and K_3BiCl_6 are shown in the Supporting Information.

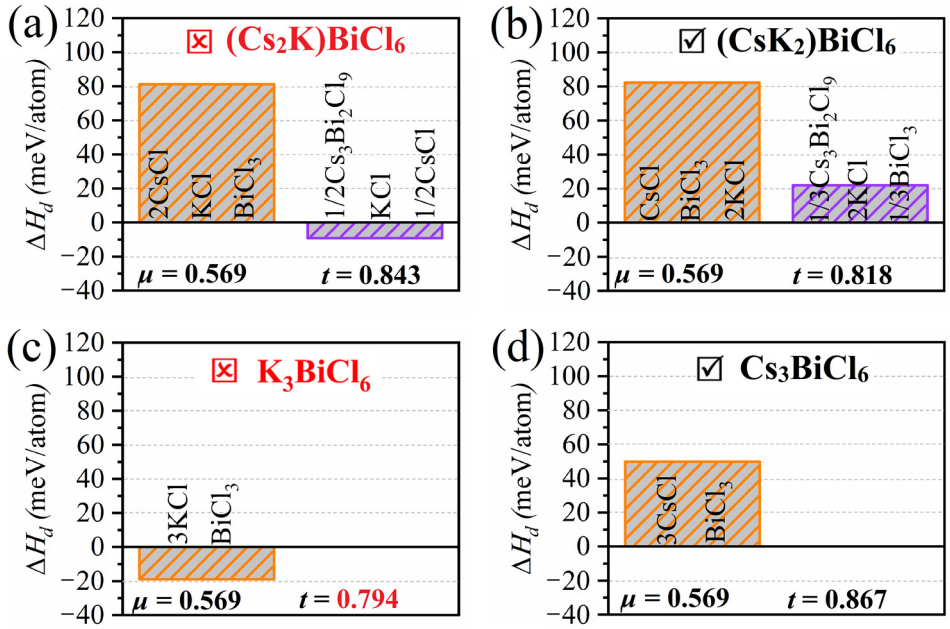

Figure 2. Calculated decomposition enthalpies (ΔH_d) of $(Cs_2K)BiCl_6$ (**a**), $(CsK_2)BiCl_6$ (**b**), K_3BiCl_6 (**c**) and Cs_3BiCl_6 (**d**). The orange bars indicate pathways involving only binary compounds. The violet bars indicate the lowest ΔH_d pathways involving ternary compounds. K_3BiCl_6 and Cs_3BiCl_6 do not involve decomposition paths for ternary compounds. The Goldschmidt tolerance factor (t) and the octahedral factor (μ) are also indicated, red indicates unsuitable values.

For the four structures, Cs_3BiCl_6, $(Cs_2K)BiCl_6$ and $(CsK_2)BiCl_6$ show positive ΔH_d values, while K_3BiCl_6 shows negative ΔH_d values in decomposition paths involving only binary compounds, indicating that K_3BiCl_6 cannot be synthesized stably (Figure 2). However, when considering ternary compounds, such as $Cs_3Bi_2Cl_9$, $(Cs_2K)BiCl_6$ shows negative values, indicating that even if $(Cs_2K)BiCl_6$ can be synthesized, it would spontaneously decompose into a mixture of $Cs_3Bi_2Cl_9$ and other binary compounds, so it is difficult to synthesize 0D $(Cs_2K)BiCl_6$ under thermodynamic equilibrium conditions. This explains why there have been no experimental reports on the successful synthesis of pure 0D $(Cs_2K)BiCl_6$ so far. For $(CsK_2)BiCl_6$, the decomposition enthalpy of $(CsK_2)BiCl_6$ is positive under the decomposition paths of all known compounds, indicating that this structure has good thermodynamic stability and may be synthesized experimentally.

2.2. Electronic Structure of $(CsK_2)BiCl_6$

The above studies show that $(CsK_2)BiCl_6$ is a stable compound, and the electronic properties of $(CsK_2)BiCl_6$ were investigated using DFT calculations. The energy band structure shows that the indirect bandgap of $(CsK_2)BiCl_6$ is 3.92 eV (Figure 3a). Combined with DOS, it can be seen that the valence band maximum (VBM) of $(CsK_2)BiCl_6$ mainly comes from the s orbital of Bi and the p orbital of Cl, while the conduction band minimum (CBM) is mainly contributed by the p orbital of Bi and Cl (Figure 3b). In the charge density of Figure 3c, whether it is HOMO or LUMO, the charge is mainly concentrated between the Bi atom and the Cl atom. This is consistent with our previously calculated results for Cs_3BiCl_6, indicating that the change of the A site has a very negligible effect on the electronic structure of Cs_3BiCl_6. However, it can effectively reduce the proportion of Cs in the compound and expand the compositional space of Bi-based halides.

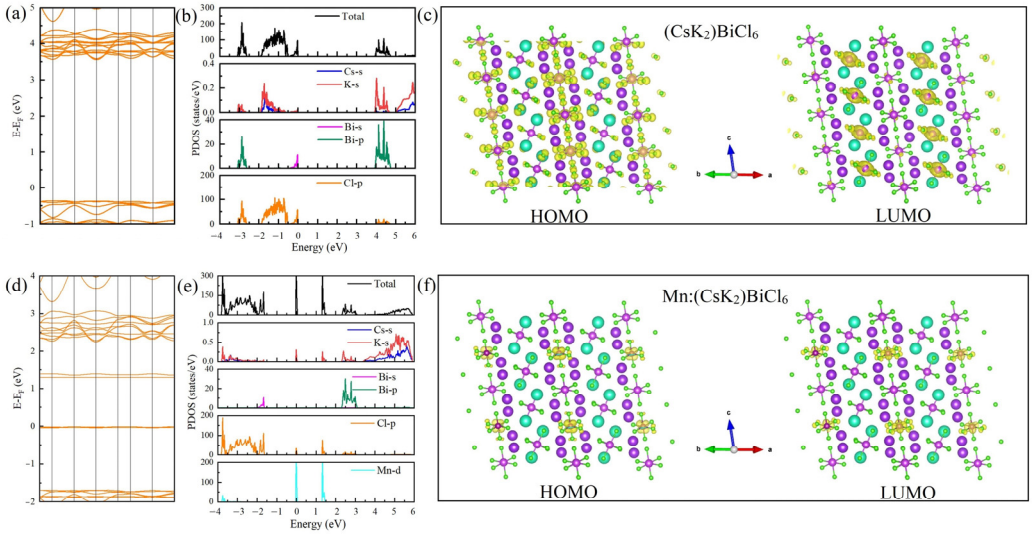

Figure 3. Calculated band structures (**a**,**d**), density of states (**b**,**e**), and charge densities (**c**,**f**) of Mn-doped and undoped $(CsK_2)BiCl_6$.

Similar to Cs_3BiCl_6, the inherent indirect bandgap of $(CsK_2)BiCl_6$ may lead to its poor PL performance, limiting its further applications. Previous research results show that doping can effectively tune the electronic structure of materials, and experimentally reasonable doping can improve the PL performance of metal halides [27,53]. As a suitable metal ion dopant, Mn^{2+} has been widely used to tune the optical properties of semiconductors. Therefore, the electronic structure of $(CsK_2)BiCl_6$ after Mn doping was calculated. We constructed an Mn-doped $(CsK_2)BiCl_6$ structure by replacing Bi with Mn and optimized it to obtain the most stable crystal structure. Figure 3d–f shows the energy band structure, DOS and charge density of Mn-doped $(CsK_2)BiCl_6$, respectively. Compared with pristine $(CsK_2)BiCl_6$, Mn-doping produces two impurity states in the forbidden band. Combining DOS, it is found that these two impurity states are mainly due to the contribution of the 3D orbital of Mn. Figure 3f shows the charge density of Mn-doped $(CsK_2)BiCl_6$. The results show that the charge density around Mn is higher than that of Bi in both HOMO and LUMO. This is mainly due to the different valence states of Mn^{2+} and Bi^{3+}, while the high charge density around Mn explains the charge balance of Mn-doped $(CsK_2)BiCl_6$.

When light passes through some solid materials, electrons, atoms or ions in the material will interact with the light, resulting in reflection, absorption and projection. The absorption of light by semiconductor materials is mainly divided into intrinsic absorption, lattice vibration absorption and carrier absorption. The absorption spectrum is calculated from the dielectric function equation [54]:

$$\alpha(\omega) = \left(\sqrt{2}\right)\omega\left[\sqrt{\varepsilon_1(\omega)^2 + \varepsilon_2(\omega)^2} - \varepsilon_1(\omega)^2\right]^{\frac{1}{2}} \quad (6)$$

where ε_1 and ε_2 correspond to the real and imaginary parts of the dielectric function, respectively. Usually, the interaction between the dopant atoms and the substrate leads to enhanced optical properties of the doped structure. Figure S1 (see in Supplementary Materials) calculates the optical absorption of undoped and Mn-doped $(CsK_2)BiCl_6$. Compared with pristine $(CsK_2)BiCl_6$, the absorption coefficient of Mn-doped $(CsK_2)BiCl_6$ moves in the lower energy direction, the absorption edge is red-shifted, and the energy corresponding to the peak of the absorption coefficient is consistent with the dielectric function (Figure S2). In the 1.2–4.4 eV region, the absorption coefficient of Mn-doped $(CsK_2)BiCl_6$ was significantly enhanced, indicating that Mn-doped $(CsK_2)BiCl_6$ has a better absorption effect on visible light.

2.3. Experimental Crystal Structure of $(CsK_2)BiCl_6$

The pristine 0D $(CsK_2)BiCl_6$ crystals were synthesized with a simple solvothermal method. The detailed experimental method is described in the supporting information. Figure S3 shows the powder X-ray diffraction (PXRD) pattern of the samples. The theoretical XRD results match well with simulated XRD patterns and show no impurity formation.

To understand the optical properties of 0D $(CsK_2)BiCl_6$, the absorption and PL spectra of the material were tested. The PL spectrum has no emission at room temperature, which may be due to the indirect bandgap properties of the material. The recombination process of the excited state band edge in the indirect bandgap material needs the assistance of phonons, making the nonradiative recombination dominant, thus, reducing the radiative recombination process, and in turn resulting in its poor PL performance [55]. Figure S4 shows the absorption spectrum and Tauc plot diagram of $(CsK_2)BiCl_6$. The absorption spectrum shows that 0D $(CsK_2)BiCl_6$ has absorption characteristics between 250 and 400 nm, especially at 260, 320 and 360 nm. These characteristic absorption peaks come from the 6s2 to 6s1p1 transition in the $BiCl_6^{3-}$ octahedron. The Tauc plot shows that the material has two linear band edge intercepts of 3.29 and 4.02 eV, respectively, which is similar to that of $Cs_2NaBiCl_6$ [56]. The experimental bandgap value of the $(CsK_2)BiCl_6$ material is 4.02 eV, which is higher than the theoretical calculation result (3.8 eV). This computed bandgap is lower than the experimentally estimated bandgap because standard DFT calculations usually underestimate the bandgap of the material.

Mn^{2+} ion is widely used for improving and regulating the optical properties and band structure of materials [57–59]. For the poor optical properties of $(CsK_2)BiCl_6$, Mn^{2+} doping is expected to enhance its luminescence and make it a candidate material for optoelectronic device applications. A series of $(CsK_2)BiCl_6$ metal halides doped with different Mn^{2+} concentrations were synthesized. The schematic structure of Mn-doped $(CsK_2)BiCl_6$ is shown in Figure 4a. Mn^{2+} ions are doped into the lattice to replace Bi^{3+} to form an isolated $MnCl_6^{4-}$ structure. The PXRD patterns of $(CsK_2)BiCl_6$ doped with different Mn^{2+} concentrations are shown in Figure 4b. The doping of Mn^{2+} ions do not show any new impurity peaks. The overall peak position is consistent with the pristine $(CsK_2)BiCl_6$. The results show that Mn^{2+} doping does not destroy the structure of the host $(CsK_2)BiCl_6$.

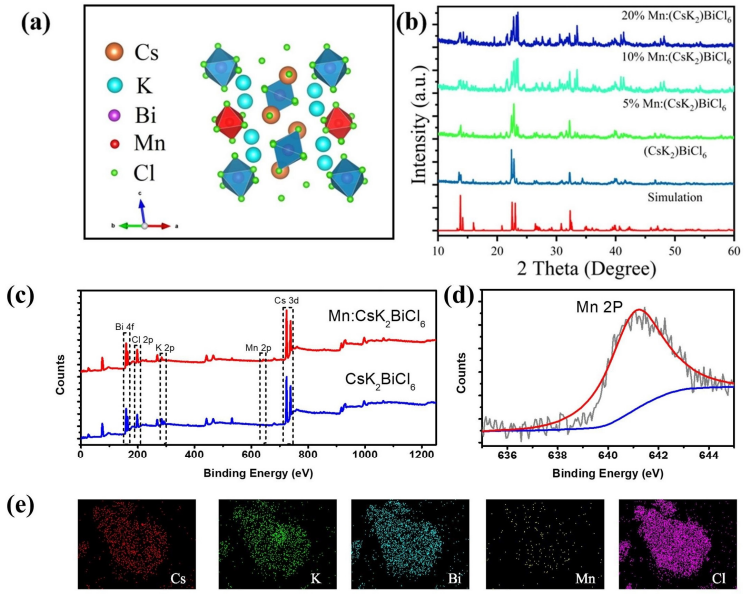

Figure 4. (**a**) The crystal structure diagram of $(CsK_2)BiCl_6$. (**b**) Power XRD patterns for Mn-doped $(CsK_2)BiCl_6$ with different Bi/Mn feed ratios. (**c**) The XPS spectra of $(CsK_2)BiCl_6$ and Mn: $(CsK_2)BiCl_6$ (Mn/Bi = 0.1). (**d**) High-resolution XPS spectra and peak fitting for Mn 2p of Mn-doped $(CsK_2)BiCl_6$ (Mn/Bi = 0.1). (**e**) EDS mapping of the Cs, K, Bi, Cl and Mn elements of Mn: $(CsK_2)BiCl_6$ (Mn/Bi = 0.1).

The X-ray photoelectron spectra (XPS) further confirmed that Mn^{2+} ions were successfully doped into $(CsK_2)BiCl_6$ and Mn^{2+} doping does not produce extra phase (Figure 4c). Figure 4d shows the high-resolution XPS spectra and peak fitting of Mn 2p. The peak at 641.0 eV is attributed to Mn 2p. Figure S5 shows the high-resolution XPS spectra of Cs, K, Bi and Cl in the samples. Compared with the pristine sample, the binding energies of Cs, K and Bi in the Mn-doped sample are slightly increased, which shows that the electron distribution of the Mn-doped samples is more compact. The composition and distribution of elements in a sample are usually determined using scanning electron microscope (SEM) images and an energy disperse spectrometer (EDS), Figures S6a and 4e are the SEM image and EDS spectra of 10%Mn: $(CsK_2)BiCl_6$, respectively. The results show that Cs, K, Bi, Cl and Mn elements are uniformly distributed in the lattice. Figure S6b shows the element content measured in selected local areas of 10%Mn: $(CsK_2)BiCl_6$ sample. The basic atomic ratio of (Cs + K):Bi:Cl is approximately 3:1:6. By using 9:1 of the nominal Bi/Mn ratio, but the actual measured Mn content is 7.5%.

2.4. Optical Properties of $(CsK_2)BiCl_6$

Previous studies have shown that the efficient luminescence center and energy transfer acceptor of Mn^{2+} ions can effectively improve the optical properties of materials. Therefore, the optical properties of the 10%Mn:$(CsK_2)BiCl_6$ sample were investigated. Figure 5a shows the absorption spectra of 10%Mn:$(CsK_2)BiCl_6$ and pristine $(CsK_2)BiCl_6$ samples, respectively. For the pristine $(CsK_2)BiCl_6$, the $BiCl_6^{3-}$ octahedrons have a strong absorption at 260, 320 and 360 nm due to the $6s^2 \rightarrow 6s^1p^1$ transition in Bi^{3+}. The 10%Mn:$(CsK_2)BiCl_6$ sample has the similar absorption characteristics as the pristine $(CsK_2)BiCl_6$ sample before 380 nm, the overall absorption peak position and shape are consistent. The main reason is that the absorption peak in this interval comes from the characteristic absorption of $BiCl_6^{3-}$ octahedrons. However, the 10%Mn:$(CsK_2)BiCl_6$ sample has an additional absorption peak at 430 and 520 nm, which is from the $^6A_{1g}$ to $^4T_{1g}$ absorption transition of Mn^{2+}. Figure 5b shows the PLE and PL spectra of 10%Mn:$(CsK_2)BiCl_6$ sample. The excitation spectra show three main excitation peaks that correspond to the absorption spectra. The excitation peaks less than 400 nm come from the transition from the ground state $^1S_0$ of Bi^{3+} to the excited states $^3P_1$ and $^1P_1$. The excitation peaks larger than 400 nm come from Mn^{2+} characteristic transitions. The PL spectra show that, compared with pristine $(CsK_2)BiCl_6$, the material achieves bright orange emission at 605 nm through Mn^{2+} doping modification. Under the excitation of different wavelengths, such as 295, 365 and 430 nm, the peak position and peak shape of the PL spectrum are consistent. In addition, the peak shapes and positions of the excitation spectra measured with different emission wavelengths remain consistent, and the results are shown in Figure S7. The PL intensity is highest under the optimal excitation wavelength (365 nm), which suggests that the observed emission is actually from the intrinsic states of the samples, rather than nonradiative transitions, such as lattice defects and surface states.

The photophysical mechanism of 10%Mn:$(CsK_2)BiCl_6$ is shown in Figure 5c. Under the excitation of UV light, the electron absorbs energy and transitions from the valence band to the conduction band. For undoped samples, due to the nature of the indirect bandgap, most of the energy is lost through phonon vibration. The carriers in the conduction band cannot be transferred to self-trapped excitons or formed into self-trapped excitons, resulting in very poor luminescent performance. For Mn-doped samples, combined with the previous theoretical calculation, Mn doping can form an impurity state in the energy band structure, and the excited state carriers can effectively relax to the $^4T_1$ state of Mn^{2+}, and transition from the $^4T_1$ state to the $^6A_1$ state, during this process, photons are emitted, and a bright orange light emission is produced. Figure S8 shows the PL spectra of pristine $(CsK_2)BiCl_6$ and x%Mn:$(CsK_2)BiCl_6$, and the pristine sample exhibits very poor optical properties. After Mn^{2+} doping, the sample exhibits a broadband emission at 605 nm, and the emission peak intensity gradually increases with increasing Mn-doping concentration. When the Mn^{2+} doping concentration is 10%, the PL intensity of the system reaches its highest. Figure 5d

shows the time-resolved PL lifetimes of 5%, 10% and 20% of Mn^{2+} doped $(CsK_2)BiCl_6$ samples monitored at 605 nm. The curve can be fitted by a double exponential function $A(t) = A_1\exp(-t/\tau_1) + A_2\exp(-t/\tau_2)$, where A(t) is the time change in PL intensity at time t, τ_1/τ_2 represents the lifetime of different recombination processes, and A_1/A_2 is the corresponding weight. The fitting data are shown in Table S1. The results show that the samples in the system exhibit a submillisecond lifetime, which is consistent with the typical characteristics of the PL lifetime of Mn^{2+} ions.

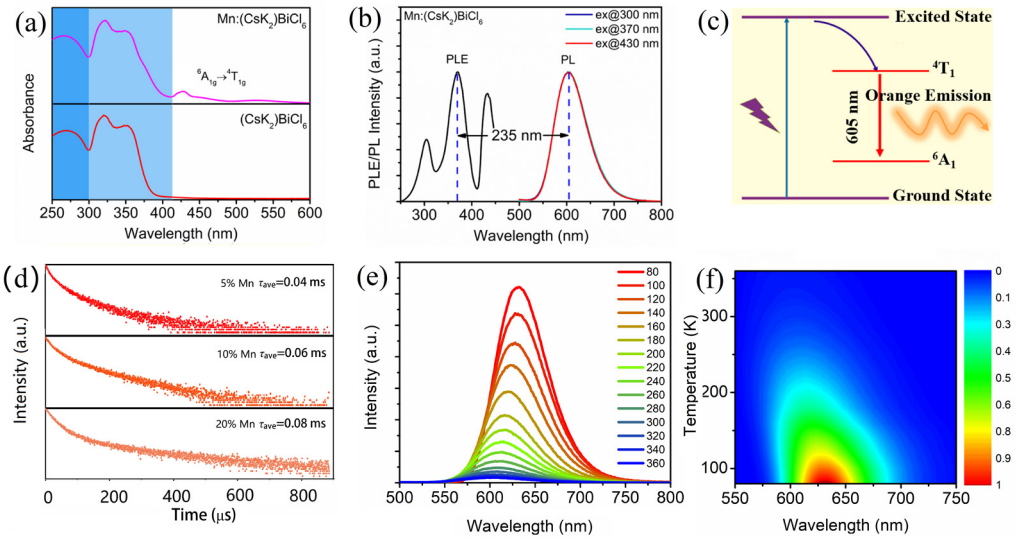

Figure 5. (**a**) The absorption spectra of $(CsK_2)BiCl_6$ and Mn:$(CsK_2)BiCl_6$. (**b**) The PL and PLE spectra of $(CsK_2)BiCl_6$. (**c**) The energy transfer diagram of Mn-doped $(CsK_2)BiCl_6$. (**d**) Time-resolved PL (TR-PL) spectra of $(CsK_2)BiCl_6$ with different Mn^{2+} doping concentrations. (**e**) Temperature-dependent PL spectra of Mn:$(CsK_2)BiCl_6$. (**f**) Pseudo color mapping of temperature-dependent PL intensity and wavelength.

The intrinsic photophysical properties of $(CsK_2)BiCl_6$ are further revealed, and the temperature-dependent emission spectra of Mn-doped systems are measured. Figure 5e shows the PL spectrum of 10%Mn:$(CsK_2)BiCl_6$ in the temperature range of 80~360 K. Similar to common metal halides, the PL intensity increases significantly at low temperatures, which is due to the weakening of electron-phonon coupling with decreasing temperature, thereby suppressing nonradiative recombination. The PL intensity decreases as the temperature increases from 80 to 360 K, which is consistent with the model that more and more phonons participate in intensifying nonradiative recombination at high temperatures. It is worth noting that the PL peak position of the sample shifted slightly with temperature. As shown in Figure S9, with the temperature increasing from 80 to 360 K, the central peak position shifted from 630 to 605 nm. This is because the increase in temperature leads to the expansion of the lattice, thereby increasing the Mn-Mn spacing. The luminescence of Mn^{2+} is closely related to the Mn-Mn spacing. The increase in spacing makes the interaction between Mn-Mn weaken, resulting in an increase in the energy level difference of $^4T_1$—$^6A_1$. Figure 5f shows a pseudo color plot of temperature-dependent PL intensity and wavelength. Compared with the PL intensity at low temperature, the luminescence quenching occurred at 300 K, indicating that the luminescence performance of the material at room temperature is poor. Figure S10 shows the full width at half maximum (FWHM) as a function of temperature, and the results show that FWHM increases significantly with increasing temperature. The electron-phonon coupling in a soft halide matrix leads to a larger FWHM with increasing temperature. However, excessive electron-phonon coupling can cause energy to be dissipated by vibrations of phonons, leading to the predominance of nonradiative recombination and degrading the luminescent properties of the material. In general, improving the optical properties of bismuth-based perovskite materials requires

solving the strong electron-phonon coupling characteristics inside the material and enhancing its exciton binding energy. How to effectively improve these two factors is the solution and strategy to solve the poor optical properties of such materials, and the design and regulation of future materials should be broken through and improved in this direction.

3. Conclusions

In summary, we apply DFT calculations to study the structure and stability of different A sites in 0D A_3BiCl_6. Theoretical analysis shows that 0D $(CsK_2)BiCl_6$ has a stable structure. We further successfully synthesized $(CsK_2)BiCl_6$ using the solvothermal method to confirm our prediction. The pristine $(CsK_2)BiCl_6$ has poor luminescence properties due to the inherent indirect bandgap feature. The successful Mn doping helps to break the forbidden transition of $(CsK_2)BiCl_6$ while maintaining the 0D structure and boosts the efficient orange emission, which comes from the efficient energy transfer from STE to d-state of Mn ions. These results enrich the family of 0D metal halides, making $(CsK_2)BiCl_6$ a new candidate for future low-toxicity and low-dimensional optoelectronic materials.

Supplementary Materials: The following supporting information can be downloaded at: https://www.mdpi.com/article/10.3390/cryst12111681/s1, Figure S1: Absorption coefficients of Mn-doped and undoped $(CsK_2)BiCl_6$; Figure S2: (a–f) Real and imaginary parts of the dielectric function, reflectivity index, refractive index, energy loss coefficient, extinction coefficient of pristine $(CsK_2)BiCl_6$ and Mn-doped $(CsK_2)BiCl_6$; Figure S3: Experimental and calculated power XRD pattern of $(CsK_2)BiCl_6$; Figure S4: The absorption spectra of $(CsK_2)BiCl_6$ and corresponding Tauc spectra; Figure S5: The high-resolution XPS spectra of Cs, K, Bi and Cl in the 10%Mn: $(CsK_2)BiCl_6$; Figure S6: (a)The SEM characterization of 10% Mn:$(CsK_2)BiCl_6$. (b) the corresponding EDS spectrum; Figure S7: The PLE spectra for different PL positions of Mn:$(CsK_2)BiCl_6$ (Mn/Bi = 0.1); Figure S8: The PL spectra of Mn:$(CsK_2)BiCl_6$ with different Mn^{2+} doping concentrations; Figure S9: Dot plot of PL peak position as a function of temperature; Figure S10: The relationship between FWHM and temperature; Table S1: The PL lifetime fitting result of $(CsK_2)BiCl_6$ with different Mn concentration.

Author Contributions: Conceptualization, J.W. and R.Z.; methodology, J.W. and J.Y.; software, S.Z.; validation, J.W.; investigation, J.W.; resources; data curation, S.Z.; writing—original draft preparation, J.W. and R.Z.; writing—review and editing, J.W. and R.Z.; supervision, B.Z. and R.Z.; funding acquisition, R.Z. All authors have read and agreed to the published version of the manuscript.

Funding: This work was supported by the National Natural Science Foundation of China [22175043, 52162021], the Natural Science Foundation of Guangxi Province [2017GXNSFGA198005], and the Innovation Project of Guangxi Graduate Education [YCBZ2022048].

Institutional Review Board Statement: Not applicable.

Informed Consent Statement: Not applicable.

Data Availability Statement: Not applicable.

Conflicts of Interest: The authors declare no conflict of interest.

References

1. Yang, H.; Cai, T.; Liu, E.; Hills-Kimball, K.; Gao, J.; Chen, O. Synthesis and transformation of zero-dimensional Cs_3BiX_6 (X = Cl, Br) perovskite-analogue nanocrystals. *Nano Res.* **2019**, *13*, 282–291. [CrossRef]
2. Akkerman, Q.A.; Raino, G.; Kovalenko, M.V.; Manna, L. Genesis, challenges and opportunities for colloidal lead halide perovskite nanocrystals. *Nat. Mater.* **2018**, *17*, 394–405. [CrossRef] [PubMed]
3. Gao, L.; Yan, Q. Recent Advances in Lead Halide Perovskites for Radiation Detectors. *Sol. RRL* **2019**, *4*, 210. [CrossRef]
4. He, T.; Li, S.; Jiang, Y.; Qin, C.; Cui, M.; Qiao, L.; Xu, H.; Yang, J.; Long, R.; Wang, H.; et al. Reduced-dimensional perovskite photovoltaics with homogeneous energy landscape. *Nat. Commun.* **2020**, *11*, 1672. [CrossRef]
5. Li, F.; Huang, S.; Liu, X.; Bai, Z.; Wang, Z.; Xie, H.; Bai, X.; Zhong, H. Highly Stable and Spectrally Tunable Gamma Phase $Rb_xCs_{1-x}PbI_3$ Gradient-Alloyed Quantum Dots in PMMA Matrix through A Sites Engineering. *Adv. Funct. Mater.* **2021**, *31*, 2008211. [CrossRef]
6. Gu, Z.; Wang, Y.; Wang, S. Controllable printing of large-scale compact perovskite films for flexible photodetectors. *Nano Res.* **2022**, *15*, 1547–1553. [CrossRef]

7. Shynkarenko, Y.; Bodnarchuk, M.I.; Bernasconi, C.; Berezovska, Y.; Verteletskyi, V.; Ochsenbein, S.T.; Kovalenko, M.V. Direct Synthesis of Quaternary Alkylammonium-Capped Perovskite Nanocrystals for Efficient Blue and Green Light-Emitting Diodes. *ACS Energy Lett.* **2019**, *4*, 2703–2711. [CrossRef]
8. Xu, Y.; Cao, M.; Huang, S. Recent advances and perspective on the synthesis and photocatalytic application of metal halide perovskite nanocrystals. *Nano Res.* **2021**, *14*, 3773–3794. [CrossRef]
9. Yuan, M.; Voznyy, O.; Zhitomirsky, D.; Kanjanaboos, P.; Sargent, E.H. Synergistic Doping of Fullerene Electron Transport Layer and Colloidal Quantum Dot Solids Enhances Solar Cell Performance. *Adv. Mater.* **2015**, *27*, 917–921. [CrossRef]
10. Wei, Z.; Yan, K.; Chen, H.; Yi, Y.; Zhang, T.; Long, X.; Li, J.; Zhang, L.; Wang, J.; Yang, S. Cost-efficient clamping solar cells using candle soot for hole extraction from ambipolar perovskites. *Energy Environ. Sci.* **2014**, *7*, 3326–3333. [CrossRef]
11. Zhuang, Q.; Wang, H.; Zhang, C. Ion diffusion-induced double layer doping toward stable and efficient perovskite solar cells. *Nano Res.* **2022**, *15*, 5114–5122. [CrossRef]
12. Zhang, F.; Zhang, X.; Wang, C.; Sun, M.; Luo, X.; Yang, Y.; Chang, S.; Zhang, D.; Duan, L. Chlorine distribution management for spectrally stable and efficient perovskite blue light-emitting diodes. *Nano Energy* **2021**, *79*, 105486. [CrossRef]
13. Chang, T.; Wang, H.; Gao, Y.; Cao, S.; Zhao, J.; Zou, B.; Zeng, R. Component Engineering to Tailor the Structure and Optical Properties of Sb-Doped Indium-Based Halides. *Inorg. Chem.* **2022**, *61*, 1486–1494. [CrossRef] [PubMed]
14. Ning, W.; Gao, F. Structural and Functional Diversity in Lead-Free Halide Perovskite Materials. *Adv. Mater.* **2019**, *31*, e1900326. [CrossRef] [PubMed]
15. Ren, M.; Cao, S.; Zhao, J.; Zou, B.; Zeng, R. Advances and Challenges in Two-Dimensional Organic-Inorganic Hybrid Perovskites toward High-Performance Light-Emitting Diodes. *Nano-Micro Lett.* **2021**, *13*, 163. [CrossRef] [PubMed]
16. Xiao, Z.; Meng, W.; Wang, J.; Mitzi, D.B.; Yan, Y. Searching for promising new perovskite-based photovoltaic absorbers: The importance of electronic dimensionality. *Mater. Horiz.* **2017**, *4*, 206–216. [CrossRef]
17. Yu, W.; Sun, X.; Xiao, M.; Hou, T.; Liu, X.; Zheng, B.; Yu, H.; Zhang, M.; Huang, Y.; Hao, X. Recent advances on interface engineering of perovskite solar cells. *Nano Res.* **2021**, *15*, 85–103. [CrossRef]
18. Hao, F.; Stoumpos, C.C.; Cao, D.H.; Chang, R.P.H.; Kanatzidis, M.G. Lead-free solid-state organic–inorganic halide perovskite solar cells. *Nat. Photonics* **2014**, *8*, 489–494. [CrossRef]
19. Lee, S.J.; Shin, S.S.; Kim, Y.C.; Kim, D.; Ahn, T.K.; Noh, J.H.; Seo, J.; Seok, S.I. Fabrication of Efficient Formamidinium Tin Iodide Perovskite Solar Cells through SnF_2-Pyrazine Complex. *J. Am. Chem. Soc.* **2016**, *138*, 3974–3977. [CrossRef]
20. Liao, W.; Zhao, D.; Yu, Y.; Grice, C.R.; Wang, C.; Cimaroli, A.J.; Schulz, P.; Meng, W.; Zhu, K.; Xiong, R.G.; et al. Lead-Free Inverted Planar Formamidinium Tin Triiodide Perovskite Solar Cells Achieving Power Conversion Efficiencies up to 6.22. *Adv. Mater.* **2016**, *28*, 9333–9340. [CrossRef]
21. Noel, N.K.; Stranks, S.D.; Abate, A.; Wehrenfennig, C.; Guarnera, S.; Haghighirad, A.-A.; Sadhanala, A.; Eperon, G.E.; Pathak, S.K.; Johnston, M.B.; et al. Lead-free organic–inorganic tin halide perovskites for photovoltaic applications. *Energy Environ. Sci.* **2014**, *7*, 3061–3068. [CrossRef]
22. Wang, C.; Bai, Y.; Guo, Q.; Zhao, C.; Zhang, J.; Hu, S.; Hayat, T.; Alsaedi, A.; Tan, Z. Enhancing charge transport in an organic photoactive layer via vertical component engineering for efficient perovskite/organic integrated solar cells. *Nanoscale* **2019**, *11*, 4035–4043. [CrossRef]
23. Fu, S.; Li, X.; Wan, L.; Zhang, W.; Song, W.; Fang, J. Effective Surface Treatment for High-Performance Inverted $CsPbI_2Br$ Perovskite Solar Cells with Efficiency of 15.92. *Nano-Micro Lett.* **2020**, *12*, 170. [CrossRef]
24. Huang, J.; Chang, T.; Zeng, R.; Yan, J.; Wei, Q.; Zhou, W.; Cao, S.; Zou, B. Controlled Structural Transformation in Sb-Doped Indium Halides A_3InCl_6 and $A_2InCl_5{\cdot}H_2O$ Yields Reversible Green-to-Yellow Emission Switch. *Adv. Opt. Mater.* **2021**, *9*, 2002267. [CrossRef]
25. Park, M.-H. 3D and 2D Metal Halide Perovskites for Blue Light-Emitting Diodes. *Materials* **2022**, *15*, 4571. [CrossRef] [PubMed]
26. Ke, B.; Zeng, R.; Zhao, Z.; Wei, Q.; Xue, X.; Bai, K.; Cai, C.; Zhou, W.; Xia, Z.; Zou, B. Homo- and Heterovalent Doping-Mediated Self-Trapped Exciton Emission and Energy Transfer in Mn-Doped $Cs_2Na_{1-x}Ag_xBiCl_6$ Double Perovskites. *J. Phys. Chem. Lett.* **2020**, *11*, 340–348. [CrossRef]
27. Zeng, R.; Zhang, L.; Xue, Y.; Ke, B.; Zhao, Z.; Huang, D.; Wei, Q.; Zhou, W.; Zou, B. Highly Efficient Blue Emission from Self-Trapped Excitons in Stable Sb(3+)-Doped $Cs_2NaInCl_6$ Double Perovskites. *J. Phys. Chem. Lett.* **2020**, *11*, 2053–2061. [CrossRef]
28. Jin, M.; Zheng, W.; Gong, Z. Unraveling the triplet excited-state dynamics of Bi^{3+} in vacancy-ordered double perovskite Cs_2SnCl_6 nanocrystals. *Nano Res.* **2022**, *15*, 6422–6429. [CrossRef]
29. Liao, K.; Li, C.; Xie, L.; Yuan, Y.; Wang, S.; Cao, Z.; Ding, L.; Hao, F. Hot-Casting Large-Grain Perovskite Film for Efficient Solar Cells: Film Formation and Device Performance. *Nano-Micro Lett.* **2020**, *12*, 156. [CrossRef]
30. Sun, C.; Jiang, Y.; Cui, M.; Qiao, L.; Wei, J.; Huang, Y.; Zhang, L.; He, T.; Li, S.; Hsu, H.Y.; et al. High-performance large-area quasi-2D perovskite light-emitting diodes. *Nat. Commun.* **2021**, *12*, 2207. [CrossRef]
31. Wang, X.; Wang, L.; Shan, T.; Leng, S.; Zhong, H.; Bao, Q.; Lu, Z.H.; Deng, L.L.; Chen, C.C. Low-Temperature Aging Provides 22% Efficient Bromine-Free and Passivation Layer-Free Planar Perovskite Solar Cells. *Nano-Micro Lett.* **2020**, *12*, 84. [CrossRef] [PubMed]
32. Zhou, G.; Liu, Z.; Molokeev, M.S.; Xiao, Z.; Xia, Z.; Zhang, X.-M. Manipulation of Cl/Br transmutation in zero-dimensional Mn^{2+}-based metal halides toward tunable photoluminescence and thermal quenching behaviors. *J. Mater. Chem. C* **2021**, *9*, 2047–2053. [CrossRef]

33. Xie, Y.; Zhou, A.; Zhang, X.; Ou, Q.; Zhang, S. Metal cation substitution of halide perovskite nanocrystals. *Nano Res.* **2022**, *15*, 6522–6550. [CrossRef]
34. Chen, H.; Wang, H.; Wu, J.; Wang, F.; Zhang, T.; Wang, Y.; Liu, D.; Li, S.; Penty, R.V.; White, I.H. Flexible optoelectronic devices based on metal halide perovskites. *Nano Res.* **2020**, *13*, 1997–2018. [CrossRef]
35. Akkerman, Q.A.; Park, S.; Radicchi, E.; Nunzi, F.; Mosconi, E.; De Angelis, F.; Brescia, R.; Rastogi, P.; Prato, M.; Manna, L. Nearly Monodisperse Insulator Cs_4PbX_6 (X = Cl, Br, I) Nanocrystals, Their Mixed Halide Compositions, and Their Transformation into $CsPbX_3$ Nanocrystals. *Nano Lett.* **2017**, *17*, 1924–1930. [CrossRef]
36. Giorgi, G.; Yamashita, K. Zero-Dimensional Hybrid Organic-Inorganic Halide Perovskite Modeling: Insights from First Principles. *J. Phys. Chem. Lett.* **2016**, *7*, 888–899. [CrossRef]
37. Lehner, A.J.; Fabini, D.H.; Evans, H.A.; Hébert, C.-A.; Smock, S.R.; Hu, J.; Wang, H.; Zwanziger, J.W.; Chabinyc, M.L.; Seshadri, R. Crystal and Electronic Structures of Complex Bismuth Iodides $A_3Bi_2I_9$ (A = K, Rb, Cs) Related to Perovskite: Aiding the Rational Design of Photovoltaics. *Chem. Mat.* **2015**, *27*, 7137–7148. [CrossRef]
38. Öz, S.; Hebig, J.-C.; Jung, E.; Singh, T.; Lepcha, A.; Olthof, S.; Jan, F.; Gao, Y.; German, R.; van Loosdrecht, P.H.M.; et al. Zero-dimensional $(CH_3NH_3)_3Bi_2I_9$ perovskite for optoelectronic applications. *Sol. Energy Mater. Sol. Cells.* **2016**, *158*, 195–201. [CrossRef]
39. Saidaminov, M.I.; Almutlaq, J.; Sarmah, S.; Dursun, I.; Zhumekenov, A.A.; Begum, R.; Pan, J.; Cho, N.; Mohammed, O.F.; Bakr, O.M. Pure Cs_4PbBr_6: Highly Luminescent Zero-Dimensional Perovskite Solids. *ACS Energy Lett.* **2016**, *1*, 840–845. [CrossRef]
40. Yan, J.; Zhang, S.; Wei, Q.; Cao, S.; Zhao, J.; Zou, B.; Zeng, R. Stoichiometry-Controlled Phase Engineering of Cesium Bismuth Halides and Reversible Structure Switch. *Adv. Opt. Mater.* **2022**, *10*, 2101406. [CrossRef]
41. Cheng, X.; Li, R.; Zheng, W.; Tu, D.; Shang, X.; Gong, Z.; Xu, J.; Han, S.; Chen, X. Tailoring the Broadband Emission in All-Inorganic Lead-Free 0D In-Based Halides through Sb^{3+} Doping. *Adv. Opt. Mater.* **2021**, *9*, 2100434. [CrossRef]
42. Shil, S.K.; Wang, F.; Lai, Z.; Meng, Y.; Wang, Y.; Zhao, D.; Hossain, M.K.; Egbo, K.O.; Wang, Y.; Yu, K.M.; et al. Crystalline all-inorganic lead-free $Cs_3Sb_2I_9$ perovskite microplates with ultra-fast photoconductive response and robust thermal stability. *Nano Res.* **2021**, *14*, 4116–4124. [CrossRef]
43. Zhang, J.; Yang, Y.; Deng, H.; Farooq, U.; Yang, X.; Khan, J.; Tang, J.; Song, H. High Quantum Yield Blue Emission from Lead-Free Inorganic Antimony Halide Perovskite Colloidal Quantum Dots. *ACS Nano.* **2017**, *11*, 9294–9302. [CrossRef]
44. Zhou, L.; Liao, J.F.; Huang, Z.G.; Wei, J.H.; Wang, X.D.; Li, W.G.; Chen, H.Y.; Kuang, D.B.; Su, C.Y. A Highly Red-Emissive Lead-Free Indium-Based Perovskite Single Crystal for Sensitive Water Detection. *Angew. Chem.-Int. Edit.* **2019**, *58*, 5277–5281. [CrossRef] [PubMed]
45. Kresse, G.; Furthmuller, J. Efficient iterative schemes for ab initio total-energy calculations using a plane-wave basis set. *Phys. Rev. B-Condens. Matter* **1996**, *54*, 11169–11186. [CrossRef]
46. Perdew, J.P.; Burke, K.; Ernzerhof, M. Generalized Gradient Approximation Made Simpl. *Phys. Rev. Lett.* **1996**, *77*, 3865. [CrossRef]
47. Diao, X.; Diao, Y.; Tang, Y. High-throughput screening of stable and efficient double inorganic halide perovskite materials by DFT. *Sci Rep.* **2022**, *12*, 12633. [CrossRef]
48. Garoufalis, C.S.; Galanakis, I.; Zeng, Z.; Hayrapetyan, D.B.; Baskoutas, S. Structural and Electronic Properties of Small Perovskite Nanoparticles of the Form ABX_3 (A = MA, DEA, FA, GA, B = Pb, Sn, X = Cl, Br, I). *Electron. Mater.* **2021**, *2*, 382–393. [CrossRef]
49. Zhao, X.; Dong, J.; Wu, D. Impact of A-Site Cations on Fluorescence Quenching in Organic–Inorganic Hybrid Perovskite Materials. *J. Phys. Chem. C.* **2021**, *125*, 11524–11531. [CrossRef]
50. Han, P.; Luo, C.; Yang, S.; Yang, Y.; Deng, W.; Han, K. All-Inorganic Lead-Free 0D Perovskites by a Doping Strategy to Achieve a PLQY Boost from <2% to 90. *Angew. Chem. Int. Ed. Engl.* **2020**, *59*, 12709–12713.
51. Dai, J.; Ma, L.; Ju, M.; Huang, J.; Zeng, X.C. In- and Ga-based inorganic double perovskites with direct bandgaps for photovoltaic applications. *Phys. Chem. Chem. Phys.* **2017**, *19*, 21691–21695. [CrossRef] [PubMed]
52. Fedorovskiy, A.E.; Drigo, N.A.; Nazeeruddin, M.K. The Role of Goldschmidt's Tolerance Factor in the Formation of A_2BX_6 Double Halide Perovskites and its Optimal Range. *Small Methods* **2019**, *4*, 1900426. [CrossRef]
53. Zeng, R.; Bai, K.; Wei, Q.; Chang, T.; Yan, J.; Ke, B.; Huang, J.; Wang, L.; Zhou, W.; Cao, S.; et al. Boosting triplet self-trapped exciton emission in Te(IV)-doped Cs_2SnCl_6 perovskite variants. *Nano Res.* **2020**, *14*, 1551–1558. [CrossRef]
54. Zhang, M.; Pan, J.; Zhou, W.; Li, A.; Ouyang, F. Direct/indirect band gap tunability in van der Waals heterojunctions based on ternary 2D materials $Mo_{1-x}W_xY_2$. *J. Phys.-Condes. Matter* **2019**, *31*, 505302. [CrossRef] [PubMed]
55. Zhou, L.; Liao, J.F.; Qin, Y.; Wang, X.D.; Wei, J.H.; Li, M.; Kuang, D.B.; He, R. Activation of Self-Trapped Emission in Stable Bismuth-Halide Perovskite by Suppressing Strong Exciton–Phonon Coupling. *Adv. Funct. Mater.* **2021**, *31*, 2102654. [CrossRef]
56. Li, H.; Pi, C.; Chen, W.; Zhou, M.; Wei, J.; Yi, J.; Song, P.; Alexey, Y.; Zhong, Y.; Yu, X.; et al. A Highly Stable Photodetector Based on a Lead-Free Double Perovskite Operating at Different Temperatures. *J. Phys. Chem. Lett.* **2021**, *12*, 5682–5688. [CrossRef]
57. Ren, J.; Zhou, X.; Wang, Y. Water triggered interfacial synthesis of highly luminescent $CsPbX_3$:Mn^{2+} quantum dots from nonluminescent quantum dots. *Nano Res.* **2020**, *13*, 3387–3395. [CrossRef]
58. Su, B.; Molokeev, M.S.; Xia, Z. Unveiling Mn^{2+} Dopant States in Two-Dimensional Halide Perovskite toward Highly Efficient Photoluminescence. *J. Phys. Chem. Lett.* **2020**, *11*, 2510–2517. [CrossRef]
59. Peng, L.; Huang, K.; Zhang, Z.; Zhang, Y.; Shi, Z.; Xie, R.; Yang, W. Bandgap- and Radial-Position-Dependent Mn-Doped Zn–Cu–In–S/ZnS Core/Shell Nanocrystals. *ChemPhysChem* **2016**, *17*, 752–758. [CrossRef]